Diurnal Cycle of Water Vapor as Documented by a Dense GPS Network in a Coastal Area during ESCOMPTE IOP2

Sophie Bastin, Cédric Champollion, Olivier Bock, Phillipe Drobinski, Frédéric Masson

Diurnal Cycle of Water Vapor as Documented by a Dense GPS Network in a Coastal Area during ESCOMPTE IOP2

SOPHIE BASTIN

Institut Pierre Simon Laplace/Service d'Aéronomie, Université Pierre et Marie Curie, Paris, France

CÉDRIC CHAMPOLLION

Laboratoire de Dynamique de la Lithosphère, Université Montpellier II, Montpellier, France

OLIVIER BOCK AND PHILIPPE DROBINSKI

Institut Pierre Simon Laplace/Service d'Aéronomie, Université Pierre et Marie Curie, Paris, France

FRÉDÉRIC MASSON

Laboratoire de Dynamique de la Lithosphère, Université Montpellier II, Montpellier, France

(Manuscript received 10 June 2005, in final form 10 May 2006)

ABSTRACT

Global positioning system (GPS) data from a dense network have been used for the analysis of the diurnal cycle of water vapor over Marseille, France, during the second intensive observation period (IOP2; 21–26 June 2001) of the Expérience sur Sites pour Contraindre les Modèles de Pollution Atmosphérique et de Transport d'Emission (ESCOMPTE) field experiment. Both tomographic analyses and integrated water vapor (IWV) contents from GPS have been used, in addition to wind profiler data and surface observations. Tomographic analysis of data from the dense GPS network and radiosondes provided the continuous temporal evolution of the vertical distribution of water vapor over the city of Marseille. The city is located on the shore of the Mediterranean Sea in southeastern France and is often under the influence of sea-breeze effects. Two different layers of breeze circulation are identified: a shallow sea breeze, blowing perpendicular to the local coastline, and a deep sea breeze, induced by the regional temperature gradient between sea and land. The origin of water vapor is shown to be mainly due to the advection of marine moist air by these sea-breeze circulations. However, the diurnal cycle of water vapor over Marseille is strongly influenced by the synoptic situation, which changes during the IOP2 (between a northerly mistral in the early stage of the IOP and an easterly wind at the end). It is shown that vertical profiles from tomographic analyses (combined with wind profiler data) allow for a proper interpretation of the diurnal cycle observed in IWV. Two-dimensional maps of IWV are also shown to complement the description of the horizontal advection of moisture by the different circulation regimes.

1. Introduction

Marseille is one of the largest French cities, with about 1 million inhabitants. Facing the Mediterranean Sea (Fig. 1), Marseille is frequently under the influence of sea-breeze circulations during summertime. These circulations play a key role in determining the local meteorological conditions [see Simpson (1994) for a review] and often lead to pollution episodes during anticyclonic situations (e.g., Kambezidis et al. 1998; Koo and Reible 1995). Marseille is also located in a mountainous area. As a consequence, both terrain heterogeneities and variable topography may induce local atmospheric circulations of various temporal and spatial scales, where maritime and topographic effects interact. In particular, the mistral is an orographically induced wind that develops along the Rhône valley (Mayençon 1982; Pettré 1982; Jiang et al. 2003) and influences the coast of southeastern France and the western Mediter-

Corresponding author address: Dr. Sophie Bastin, IPSL/Service d'Aéronomie, Université Pierre et Marie Curie, Boite 102, Tour 45-46, 3eme étage, 4 place Jussieu, 75252 Paris, CEDEX 05, France.
E-mail: sophie.bastin@aero.jussieu.fr

DOI: 10.1175/JAM2450.1

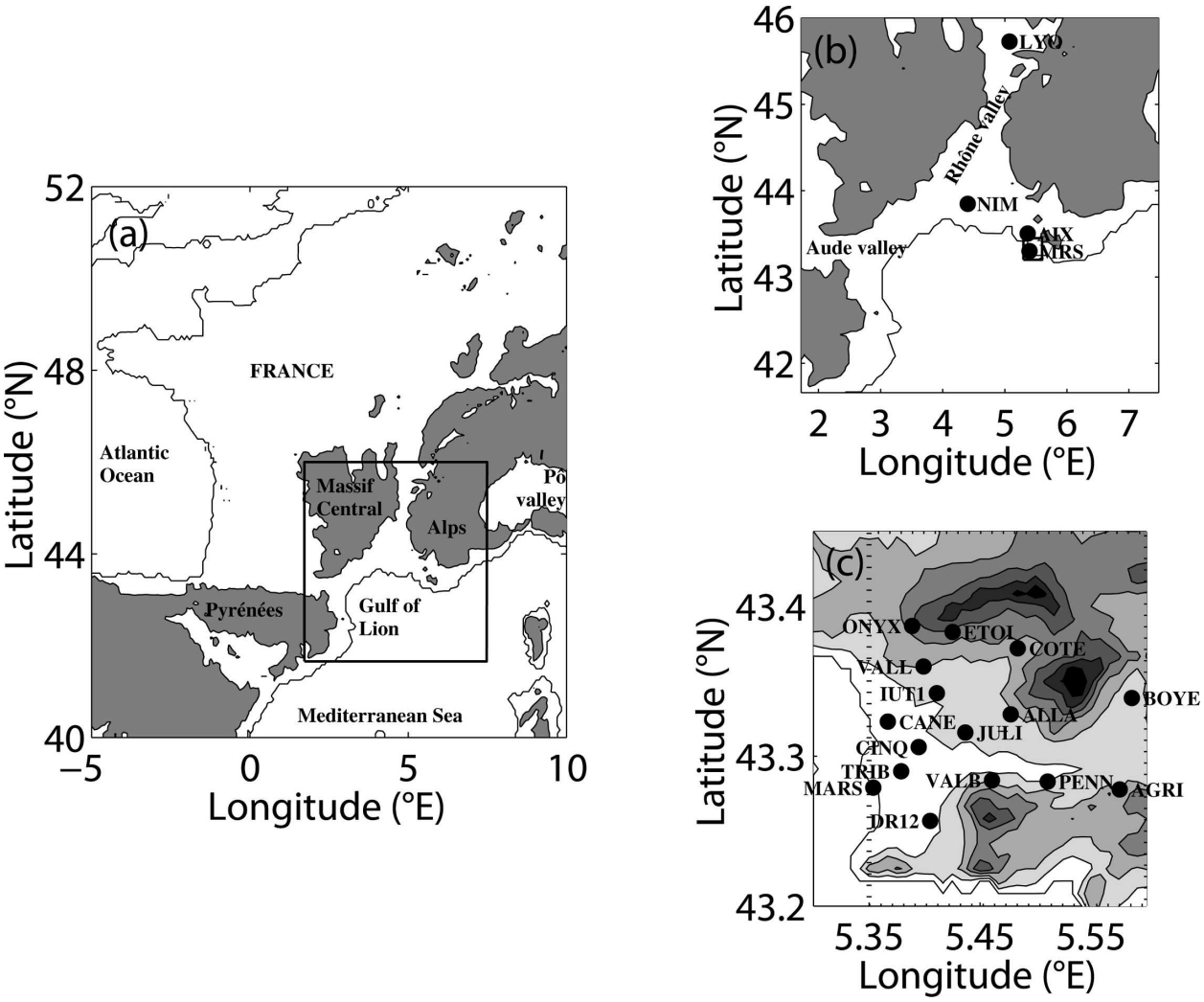

FIG. 1. (a) Map of France with the topography shaded in gray when higher than 500 m MSL. (b) Zoom of the region shown with a rectangle in (a). The acronyms AIX, LYO, NIM, and MRS correspond to the respective city names Aix-les-Milles, Lyon, Nîmes, and Marseille. The rectangle around MRS displays the limits of the GPS network deployed in the city of Marseille. (c) The Marseille GPS network. The 17 GPS receivers have a mean distance between them of about 5 km, and their associated acronyms correspond to district names or building names of the city. Filled contours of topography are indicated with an increment of 100 m. The dashed rectangle indicates the limits of the domain represented in Fig. 6.

ranean climate. It is frequently observed to extend as far as a few hundred kilometers from the coast (Jànsa 1987). Sometimes the weakness of the mistral allows the sea breeze to break through along the coast (Bastin et al. 2006; Guénard et al. 2005). The complex interaction among land/sea breezes, slope winds, and larger-scale winds (e.g., mistral) significantly affects the three-dimensional (3D) water vapor distribution and its variability and the local dynamics of convection.

The Expérience sur Sites pour Contraindre les Modèles de Pollution Atmosphérique et de Transport d'Emission (ESCOMPTE) program took place in the region of Marseille during the summer of 2001 (Cros et al. 2004). The instrumental setup allowed for the documentation of the dynamics and chemistry over the region. In particular, it was well suited to observe and investigate several mistral cases, sea-breeze cases, and also the dynamics of the interaction between the sea breeze and the mistral (Bastin et al. 2006). Moreover, during this experiment, a dense global positioning system (GPS) network was deployed in the region for the study of the variability of atmospheric water vapor (Bock et al. 2004). This network gives access to two types of products. The first one is integrated water vapor (IWV). It is usually used to analyze the temporal variability of total column humidity at each station.

Horizontal maps can be constructed from spatial interpolation of IWV between stations. However, the IWV content does not indicate where the water vapor is located in the atmospheric column. GPS tomography allows for the retrieval of both the vertical and horizontal distributions, as well as the temporal evolution of water vapor in the lower troposphere. It is a recent technique that requires GPS observations from a dense network. The network deployed during the ESCOMPTE campaign was specifically designed to allow for tomographic analysis.

The goal of the paper is to study how the synoptic situation influences the diurnal cycle of the migration of moisture over Marseille. The GPS network and its derived products of IWV and tomography make this study possible. The study will help in the scientific understanding of water vapor transport in this region, which is not well known because of the lack of water vapor observations. This study is limited to a 6-day period, corresponding to the second intensive observing period (IOP2) of the experiment, which covered two different synoptic situations. The first is an alternation of sea breeze and mistral wind, and the second is an alternation of sea breeze and land breeze.

Section 2 presents the instrumental setup and the different products obtained from the GPS network, and section 3 presents the meteorological situation. The analysis of the diurnal cycle of water vapor as a function of the synoptic situation is described in section 4. Section 5 concludes this study.

2. Measurements and data analysis

a. Instrumental setup

During the summer of 2001, meteorological measurements were taken in southern France (see Fig. 1) in the framework of ESCOMPTE (Cros et al. 2004). In the study presented here, we use the measurements from a meteorological surface-station network, radiosondes, UHF radar, and a GPS network (Bock et al. 2004) located within the city of Marseille (Fig. 1c).

Radiosondes were launched from Aix-les-Milles (see AIX in Fig. 1b), located 25 km to the north of Marseille, several times per day. On some rare days, some radiosondes were also launched from the center of Marseille.

The UHF wind profiler was located in the center of the city of Marseille, close to the GPS station named CINQ (Fig. 1c). The measurements consist of the time evolution of vertical profiles of the three wind components, including one vertical beam and two oblique beams, slanted at an off-zenith angle of 17°, the half-power beamwidth being 8.5°. The radar works with a frequency of 1238 MHz and a peak power of 4 kW. The wind velocity is estimated from the frequency corresponding to the mean Doppler shift obtained in the radar echo. The data quality control and processing are carried out through a consensus algorithm based on time and height continuity of measured spectra. The consensus works over a 60-min period, providing a wind profile every 15 min from a height of 100–300 m up to 2500–4000 m above ground level (AGL). The vertical resolution is typically 75–150 m. The errors on the horizontal wind measurements are 1–2 m s^{-1}.

The GPS network consisted of 17 GPS receivers with a mean distance between them of about 5 km (see the box in Fig. 1b). The network was designed to provide data for the validation of a tomographic analysis model developed at Laboratoire de Dynamique de la Lithosphère (Champollion et al. 2005). GPS tomography also proved to be ideally appropriate for validation of fine-scale numerical simulations of water vapor fields (Bastin et al. 2005). For this study, tomographic fields are retrieved with a 30-min interval, a horizontal grid mesh of 0.05°, and a vertical cell size ranging from 500 m near the ground to 1000 m at 10-km altitude.

b. GPS water vapor retrieval

The basic GPS atmospheric product is the tropospheric delay. This quantity is a measure of delay of the GPS signal that has traveled between a GPS satellite (at an altitude of 20 200 km) and a ground-based receiver with respect to propagation in a vacuum. The standard procedure for GPS data analysis assumes that the delay in any direction can be mapped from the delay at zenith to which a horizontal gradient is added. Three sets of parameters are then estimated during the analysis: zenith tropospheric delays (ZTDs), gradients, and postfit residuals, which are the difference between the modeled atmosphere and the measurements.

From the ZTD, the dry-atmosphere component is removed and the remainder is converted into IWV. ZTD is thus mapped into IWV, using simply surface pressure and temperature and empirical formulas (Davis et al. 1985; Bevis et al. 1992; Emardson and Derks 1999). The accuracy in GPS IWV has been assessed by a number of authors, using intercomparisons with radiosondes, microwave radiometers, sun photometers, lidars, and very long baseline interferometry (Foelsche and Kirchengast 2001; Niell et al. 2001; Bock et al. 2004). The agreement between these techniques is about 1–2 kg m^{-2}.

For the tomographic analysis of tropospheric water vapor, slant integrated water vapor (SIWV) contents are required. These contents are retrieved from a post-processing of GPS ZTD, gradient and residual estimates. First, slant delays are reconstructed by mapping

ZTD and gradients into the direction of the GPS satellites. Then, the dry atmosphere is removed. The procedure is the same as for IWV but an estimate of the dry gradient is required. Therefore, 2D surface pressure measurements are used, following Elòsegui et al. (1999). Last, the postfit residuals are added and corrected by using stacking maps (Shoji et al. 2004).

The tomographic analysis consists of retrieving the scalar three-dimensional field of water vapor density from the integrated quantities. Because we consider the geometrical effect of the bending of the ray as negligible for elevation angles higher than 10° (Elgered 1993), the problem becomes linear. The formulation in the linear discrete theory of the direct problem expresses the link between the observations (SIWV) $\mathbf{Y}$ and the true water vapor density $\mathbf{X}$ (g m^{-3}) through the linear operator $\mathbf{M}$:

$$\mathbf{Y} = \mathbf{M}\mathbf{X} + \mathbf{E}, \tag{1}$$

where $\mathbf{E}$ is the measurement error vector. The linear operator $\mathbf{M}$ is expressed as a matrix whose coefficients represent the length of each ray in each cell.

To solve the inverse problem, the matrix $\mathbf{M}$ must be inverted. Because the problem is locally underdetermined, we have to find the "generalized inverse" $\mathbf{M}^{-g}$ to obtain the reconstructed field $\mathbf{X}_{\text{reco}}$ from the data $\mathbf{Y}$:

$$\mathbf{X}_{\text{reco}} = \mathbf{M}^{-g}\mathbf{Y}. \tag{2}$$

To minimize the ill conditioning, some constraints can be added using external water vapor measurements such as humidity profiles from radiosoundings as shown in the following. More details about the processing procedure for the ESCOMPTE GPS data can be found in Walpersdorf et al. (2004) and Champollion et al. (2005). The latter reference also presents a validation of tomographic retrievals from ESCOMPTE data.

The GPS tomography without vertically resolved data assimilated allows one to retrieve the 3D field of water vapor density with limitation on the vertical resolution because of the geometrical configuration of the GPS network. Indeed, if the lateral variations of density can be resolved, several studies have shown that some structures could never be imaged, whatever the number of GPS stations in the network (Leveque and Masson 1999; Champollion et al. 2005). Several different vertical distributions of water vapor density above the highest GPS station could fit the tomographic inversion. Nevertheless, the GPS tomography provides a realistic (which may be different from the truth) vertical distribution of water vapor density that is not constant. The topography is indeed contributing to a good resolution, but only in the lowest levels (Flores et al. 2000; Champollion et al. 2005). However, given a realistic a priori model, the tomography reproduces the water vapor fields that satisfy the condition that as much moisture is mapped to the lower levels above the highest GPS station as possible given the observations. Thus, the model represents the minimum boundary layer height that is possible. The tomography shows a *possible* model that fits the data. The assimilation of vertically resolved data such as radiosondes or lidar profiles is therefore necessary to discuss the real variations of water vapor above 1 km AGL. Indeed, Fig. 2 shows a comparison between the tomography with (Fig. 2a) and without (Fig. 2b) the assimilation of radiosondes. The differences between the two fields are represented in Fig. 2c. Both the diurnal cycle (timing of the increase in boundary layer moisture) and the content of moisture at all levels differ.

The tomography is done with the software "LOFTT$_K$" developed in the Laboratoire Dynamique de la Lithosphère (Champollion et al. 2005). Some improvements have been added since its development. First, Kalman filtering has been implemented to follow the time variations of the water vapor. Second, the software allows for the assimilation of water vapor profiles from various instruments. This capability has been used only with the radiosonde data to constrain the vertical distribution of water vapor. Other data, such as radio occultation, lidar, and radiometer profiles, could be assimilated in the same way.

The Kalman filter is only used as an assimilation tool; the model for the temporal transition between two consecutive times is an identity matrix without any physical equations. The initialization of the filter is done by an interpolation of the radiosondes available at the closest release time. The initialization of the model error is done following Gradinarsky (2002), with an exponential law and a characteristic height scale of 3 km. The correlation of the errors σ of the initial model is modeled as a Gaussian function with a horizontal characteristic scale $dx_0 = 25$ km and a vertical characteristic scale $dz_0 = 500$ m to reflect the high vertical variability of the water vapor density:

$$\mathbf{C}_{X(t=t_0)}(i, j) = \sigma_i \sigma_j e^{-(dx/dx_0)^2} e^{-(dz/dz_0)^2}, \tag{3}$$

where $\mathbf{C}_{X(t=t0)}$ is the matrix of covariance of the initial model errors and dx and dz are, respectively, the horizontal and vertical distances between the two cells i and j. The choice of the initial model is not critical because the initial model is used only in the first inversion and the start time of the filter is near a radiosonde launch.

At each correction step all of the available GPS and radiosonde data are assimilated to correct the previous

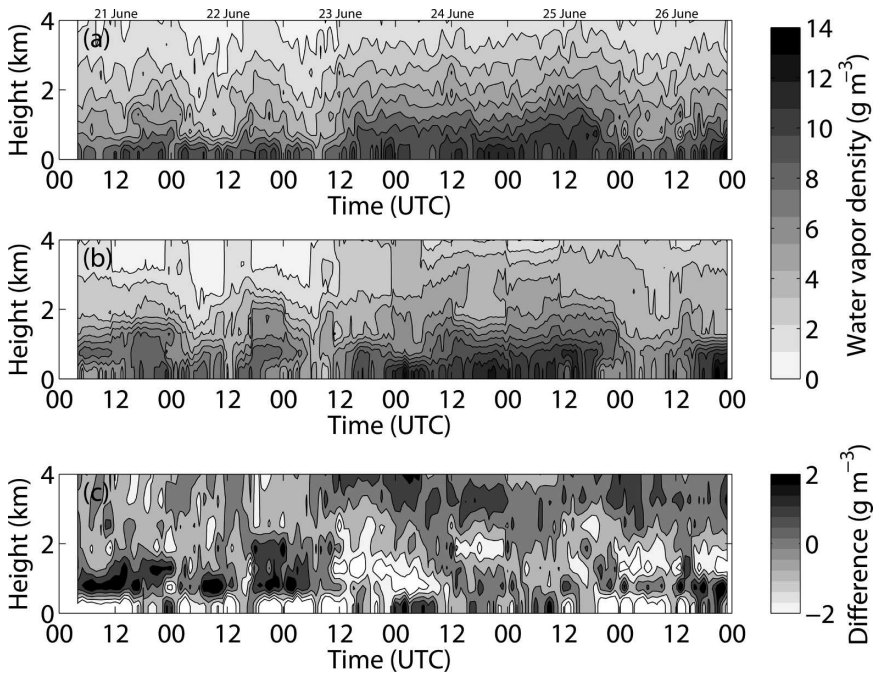

FIG. 2. Time-vs-height plot of water vapor density retrieved from GPS tomography between 21 Jun (yearday 172) and 26 Jun (yearday 177) within the center of Marseille at the CINQ station: (a) tomographic profiles obtained without assimilation of radiosondes, (b) tomographic profiles obtained with the assimilation of radiosondes, and (c) the difference between (b) and (a).

model. The measurement error covariance can be split into two different parts: the discretization and the observation (ZTD GPS estimate and errors in the conversion to SIWV). The discretization error (based on direct modeling of real data into different grids) shows a white-noise level of 2 mm for 0.05° × 0.05° × 500-m cells, with no bias and no correlation. The ZTD error (typically 6 mm) is projected to the direction of the ray path. The error of the GPS data and the conversion from delay to integrated water vapor density is a compilation of all of the errors from the previous references about the GPS data processing projected from the zenith to the elevation angle of the slant with the Niell mapping function. The correlations of the GPS slant errors σ are assumed only on the zenith measurements (not in the gradient or in the residuals) depending on the time separation dt between the two slants and the distance d between the two GPS sites:

$$\mathbf{C}_{\mathrm{SIWV}}(i, j) = \sigma_i \sigma_j e^{-(d/d_0)} e^{-(dt/dt_0)}, \tag{4}$$

where $\mathbf{C}_{\mathrm{SIWV}}$ is the matrix of covariance of the SIWV and d_0 and dt_0 are the characteristic length scale and time scale, respectively. Following the rare studies about GPS error correlation (Jarlemark et al. 2001; Haase et al. 2003), we chose $d_0 = 50$ km for the horizontal exponential correlation scale and $dt_0 = 60$ min for the time scale. The radiosounding errors are assumed to be uncorrelated. The radiosounding dataset for the six days of the study is composed of 19 radiosoundings. Sixteen of them are located in Aix-les-Milles, 25 km to the north of Marseille, and three are located near the GPS station CINQ in the center of the GPS network. The error is the sum of the measurement errors and a factor of 10 corresponding to the expected variability of the water vapor field within the tomographic cell. A radiosounding influences a cell with a Gaussian law function of the distance d between the center of the cell and the position of the radiosounding and of the difference of time dt between the radiosounding and its assimilation:

$$W = e^{-(d/d_0)^2} e^{-(dt/dt_0)^2}, \tag{5}$$

where W is the weight of a radiosonde data. The characteristic scales are $d_0 = 50$ km and $dt_0 = 60$ min for distance and time, respectively. The grid follows the terrain topography to avoid variation of the depth of the first level. The Kalman filter is updated every 30 min. Because the GPS SIWV are evaluated every 5 min with about eight satellites in view for each of the 18

GPS stations, about 900 integrated water vapor slants rays are assimilated every 30 min.

At each prediction step, the model error is increased to allow for the variation of the model within time. The increase of the model error is dynamically controlled by the error between the predicted model and the measurements: the farther away the predicted model is from measurements, the more the background error is dilated. The technique allows for dynamically adapting the filter to the slow or rapid variations of the real 3D field of water vapor.

The assimilation scheme seems to be working sufficiently well (with enough degrees of freedom) for the GPS data to influence the radiosounding data without discontinuity. The tomography fits well with the data in place and time of the radiosounding launch. During the 6 days of the IOP2, we have compared the radiosoundings and the tomographic results. With or without assimilation, no bias is found. The standard deviation is equal to about 1 g m^{-3} without assimilation and better than 0.5 g m^{-3} with the assimilation scheme. The residual standard deviation between the tomography with the radiosounding assimilated is due to errors in the SIWV and the water vapor variability for the radiosounding from Aix-les-Milles (25 km to the north of the GPS network).

3. The intensive observing period IOP2: 21–26 June 2001

During IOP2, two kinds of situations were encountered. The first 3 days of the IOP2 (hereinafter called IOP2a)—21, 22, and 23 June 2001—the mistral dominated. The mistral is a dry northwesterly flow channeled within the Rhône valley (Fig. 1). During IOP2a, it blows at night within a 2-km-deep layer and is lifted up during the day as the southwesterly sea breeze penetrates inland beneath the mistral flow (Bastin et al. 2006; Guénard et al. 2005). During the last 3 days of the IOP2 (hereinafter called IOP2b)—24, 25, and 26 June 2001—northeasterly land breeze at night alternates with sea-breeze flow during the day.

a. IOP2a (21–23 June 2001): Interaction of the sea breeze with the mistral

Figures 3a and 3b present the synoptic charts at 0000 and 1200 UTC 22 June, respectively. Note that the synoptic situation of the other days of IOP2a is similar to that of 22 June, and therefore it is the only day presented here. The IOP2a mistral event features a northwesterly flow over France resulting from an anticyclone over western France and a low pressure system over northern Europe. At 0000 UTC 22 June (Fig. 3a), a high surface pressure zone (1020 hPa) is located north and west from Ireland and extends over France, contributing to very weak surface winds upstream of the Massif Central and the Alps. In southeastern France, a cyclone is visible in the Gulf of Genoa, which is a classic mistral situation. However, it remains weak with respect to other mistral events (see, e.g., Guénard et al. 2005; Drobinski et al. 2005). It extends from the Pyrénées to the Pô valley (see Fig. 1). At 1200 UTC 22 June (Fig. 3b), the Genoa cyclone is removed but the curvature of the isobars remains, thereby causing a surface pressure gradient that is favorable to large cyclonic curvature of the mistral at the exit of the Rhône valley. Figures 4a and 4b display the wind and temperature fields from meteorological surface stations at 0000 and 1200 UTC 22 June, respectively. They clearly show the intensification of the northerly flow in the Rhône valley and the area sheltered from the mistral in the wake of the Alps (eastern side of the considered area). Note that at 1200 UTC, no sign of the sea breeze is visible in the Rhône valley delta.

b. IOP2b (24–26 June 2001): Alternation of sea breeze and land breeze

Figures 3c–f present the synoptic charts on June 25 (Figs. 3c,d) and June 26 (Figs. 3e,f) at 0000 UTC (Figs. 3c,e) and 1200 UTC (Figs. 3d,f). The situation on 24 June is similar to that on 25 June and is not presented here. At the beginning of this period, a ridge extends from Morocco to Norway. It generates a northwesterly synoptic wind at 500 hPa over southern France. On 25 June, the surface pressure is high, inducing anticyclonic conditions. At 850 hPa (not shown), the pattern indicates no significant pressure gradient over France and the Mediterranean Sea. These conditions are propitious to the development of a sea-breeze circulation. Figures 4c and 4d display the wind and temperature fields from meteorological surface stations at 0000 and 1200 UTC 25 June, respectively. Figure 4c shows no significant surface temperature gradient. At 1200 UTC (Fig. 4d), a temperature gradient appears near the coastline that drives the sea-breeze flow.

On June 26, the ridge at the 500-hPa level remains over France, but the surface high pressure moves eastward. The synoptic flow consequently weakens and veers from the northwest on 25 June to the west on 26 June. At 1200 UTC (Fig. 3f), a surface low pressure is located over southern Ireland, generating southerly low-level winds over France. Figure 4f clearly shows the combination between the sea-breeze flow generated by the temperature gradient near the coastline and the

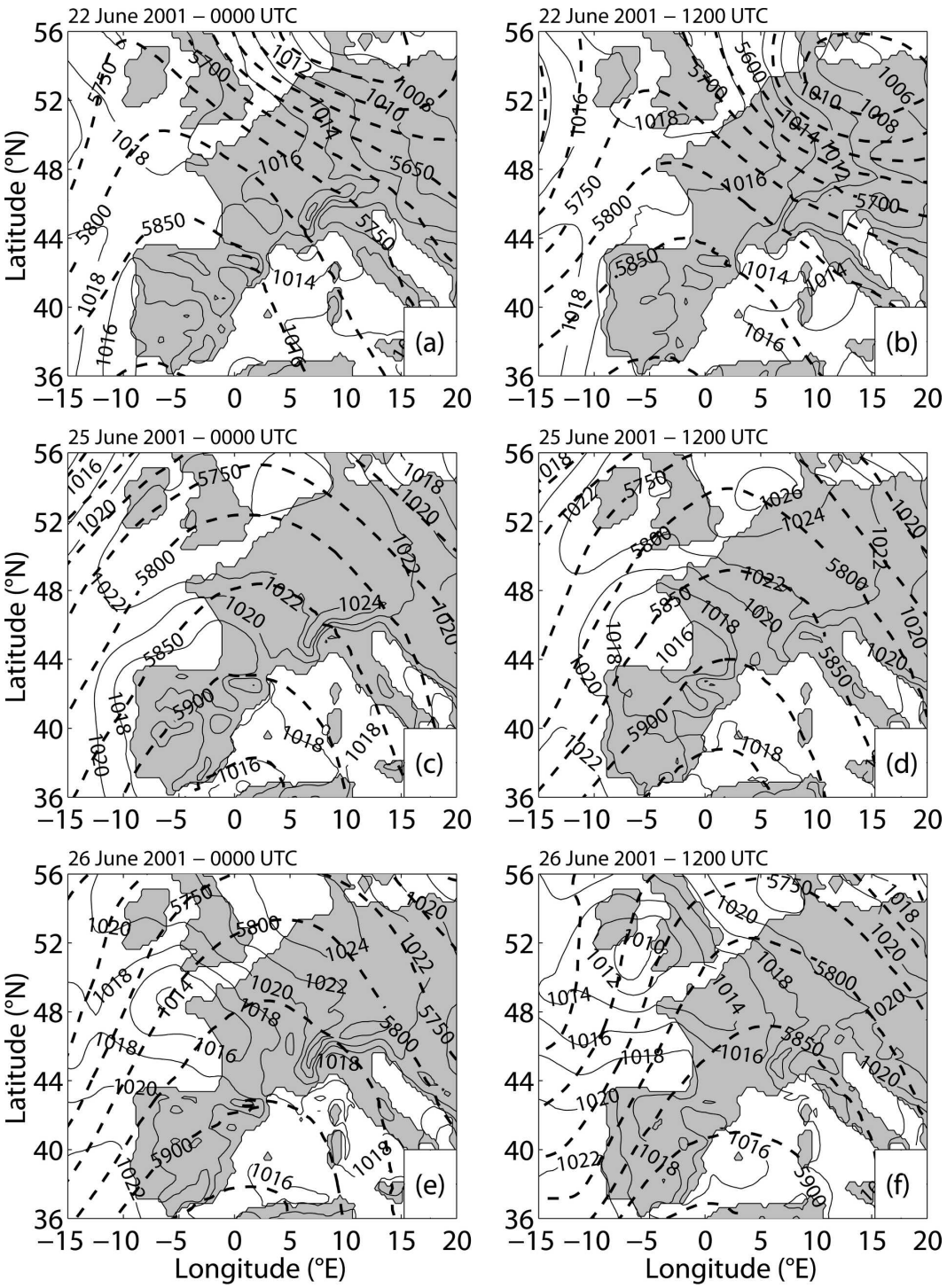

FIG. 3. Synoptic situation in 12-hourly intervals at (a) 0000 and (b) 1200 UTC 22 Jun, (c) 0000 and (d) 1200 25 Jun, and (e) 0000 and (f) 1200 UTC 26 Jun 2001 from European Centre for Medium-Range Weather Forecasts analyses. The mean sea level pressure (contour interval is 2 hPa; solid lines) and 500-hPa geopotential heights (contour interval is 50 m; thick dashed lines) are shown.

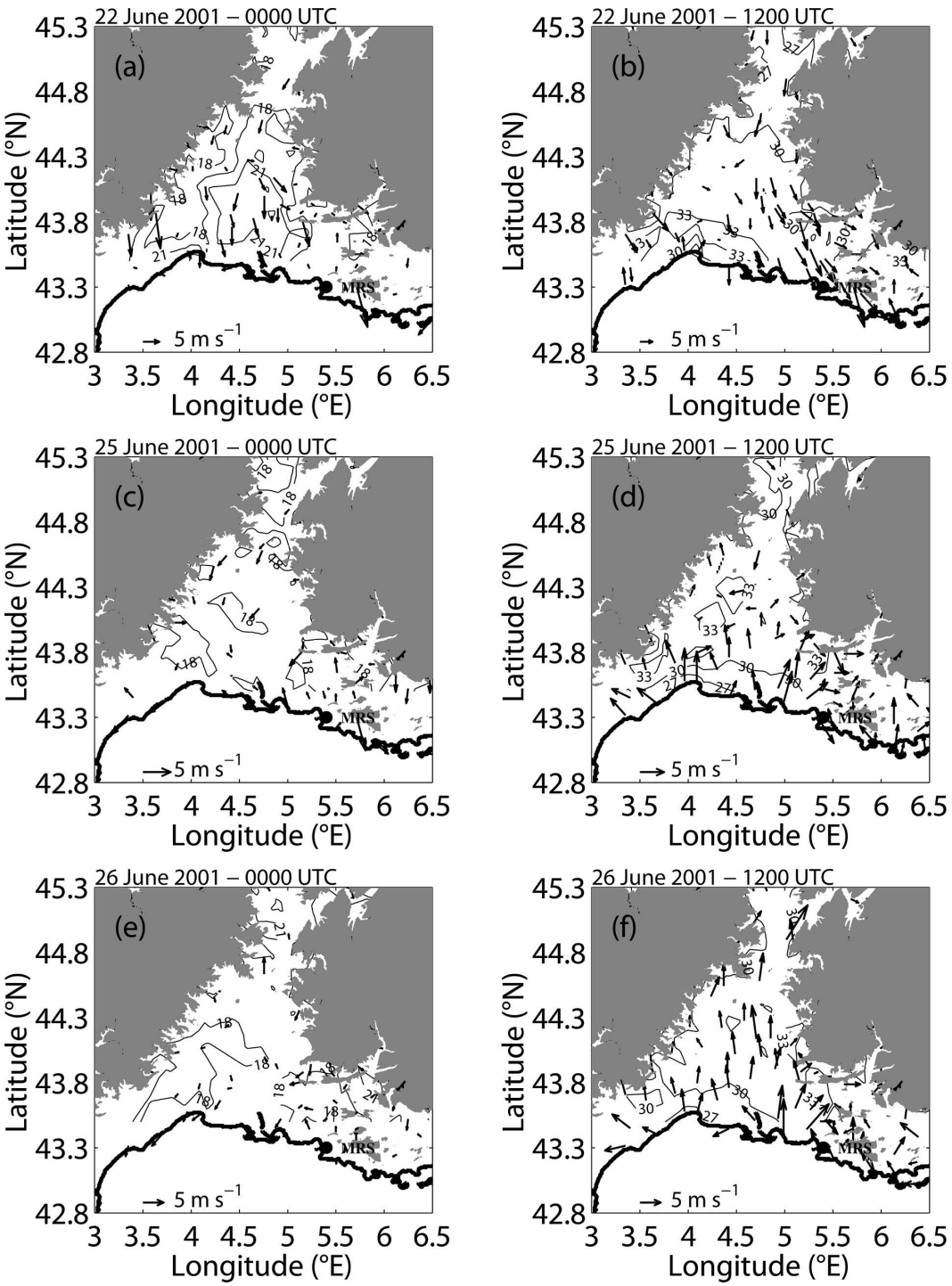

FIG. 4. Wind and temperature fields from meteorological surface stations at (a) 0000 and (b) 1200 UTC 22 Jun, (c) 0000 and (d) 1200 UTC 25 Jun, and (e) 0000 and (f) 1200 UTC 26 Jun 2001. The topography mask corresponds to topographical elements higher than 500 m MSL. The arrows indicate the wind direction, and their scale indicates the intensity. The isolines indicate the temperature. Contour interval is 3°C from 15° to 36°C. The acronym MRS indicates the location of Marseille.

southerly synoptic flow. Based on the above observations, a pollution episode was predicted to occur during IOP2b (24–26 June 2001).

c. Vertical structure of the airflow over Marseille

Figures 5a and b display vertical profiles of wind speed and wind direction, respectively, as a function of time from UHF profiler measurements over Marseille between 21 and 26 June. The UHF profiler was located in the center of the city, near the CINQ GPS station (see Fig. 1c). This figure clearly shows the differences and the transition between IOP2a and IOP2b.

During IOP2a, the diurnal cycle is well marked. Between 0000 and 1200 UTC, the wind direction is north-northwesterly from the ground up to 2 or 3 km. In this layer, the wind speed ranges from 3 to 5 m s^{-1} near the ground and can reach 20 m s^{-1} at 1-km height and above. These observations provide evidence that the whole layer between the surface and 3 km is affected by the presence of the mistral, whose intensity is weaker near the surface because of friction. During the afternoon, two different layers are apparent. In the first layer, that is, from the surface up to about 600 m AGL, the wind direction is westerly–southwesterly, associated with wind speeds of about 5–8 m s^{-1}, while in the second layer, that is, from 600 m up to 2–3 km, the wind direction is again north-northwesterly, associated with an intensity of 7–12 m s^{-1}. The existence of these two layers indicates the onset of the sea breeze in the afternoon (i.e., at about 1100 UTC 21 June, at about 1500 UTC 22 June, and at about 1300 UTC 23 June) near the coastline that lifts the mistral up to 700 or 800 m. The weakness of the mistral during this period allows the sea breeze to break through near the coastline where the temperature gradient between land and sea is maximum. Thus, during IOP2a, the mistral that blows near the surface during nighttime is not strong enough to inhibit the sea breeze (Arritt 1993) and is replaced by a sea-breeze flow near the surface during the afternoon.

The transition between IOP2a and IOP2b occurs during the afternoon of 23 June, when the mistral weakens as a result of the dissipation of the Genoa cyclone near the surface. During IOP2b, the diurnal cycle is not as well marked as during IOP2a. The wind speed is nearly the same during nighttime and daytime, even though we can distinguish a light intensification of the wind during the afternoon, and it is homogeneous with height. It ranges from 1 to 5 m s^{-1} from the ground up to 2 km. However, the wind direction shows the existence of a diurnal cycle, especially near the surface where the wind alternates from westerly during daytime to easterly during nighttime. Here we can distinguish several layers. Between the surface and about 300–400 m AGL the wind blows perpendicular to the shoreline (see Fig. 1 for the coastline shape), that is, from the west during the day (sea breeze) and from the east during night (land breeze). This direction near the surface is due to the local sea breeze, which follows the local maximum temperature gradient direction. This sea breeze is called the shallow sea breeze (SSB; Banta 1995; Bastin and Drobinski 2006; Lemonsu et al. 2006). It starts blowing at about 1000 UTC 24 and 25 June and at about 1200 UTC 26 June. Above, from about 400 m AGL up to 1300 m, the wind direction is not the same during the whole IOP2b. On 24 June, the synoptic situation induces a northwesterly flow in this second layer. On 25 June, during the day, the wind has a southerly direction corresponding to the direction of the mesoscale temperature gradient that drives the "deep sea breeze" (DSB), which blows above the SSB (Bastin and Drobinski 2006; Lemonsu et al. 2006). During the night and in the morning, this DSB does not exist and a westerly flow blows. On 26 June, the synoptic wind blows from the east. It has been shown that, on 26 June the low-level air mass, up to 2 km AGL, skirts the Mediterranean coast over land from the east-southeast (Lemonsu et al. 2006).

4. Water vapor diurnal cycle over Marseille

a. Vertically resolved water vapor

Figure 5c shows vertical profiles of water vapor density versus time from GPS tomography over Marseille, at 43.325°N latitude and 5.375°E longitude. The vertical distribution and diurnal variation of water vapor are clearly different between IOP2a and IOP2b. A strong diurnal modulation is observed during IOP2a, whereas this modulation has a smaller amplitude and is limited to a shallower layer during IOP2b. During IOP2a, a strong vertical gradient of water vapor exists in the first 3 km with values ranging from 9–10 g m^{-3} for the maximum (light blue) to 0–2 g m^{-3} (red colors) below 3 km. The thickness of this layer where all of the water vapor is concentrated (all colors except red) has a marked diurnal cycle. It ranges from 1.7–2.0 km in the late night and morning to 3.0 km in the afternoon. The maximum values of water vapor density near the surface show the same diurnal variation, with a maximum of about 9–10 g m^{-3} in the afternoon and a minimum of about 4 g m^{-3} in the late morning. During IOP2b, two different layers that both contain water vapor are apparent. The lower layer (blue, green, and yellow colors) is not homogeneous with height. The values range from 12–13 g m^{-3} near the surface to 6–7 g m^{-3} at about 1.5–2.0 km. This layer is located below a drier and more homogeneous layer of 2–4 g m^{-3} (light brown and orange colors),

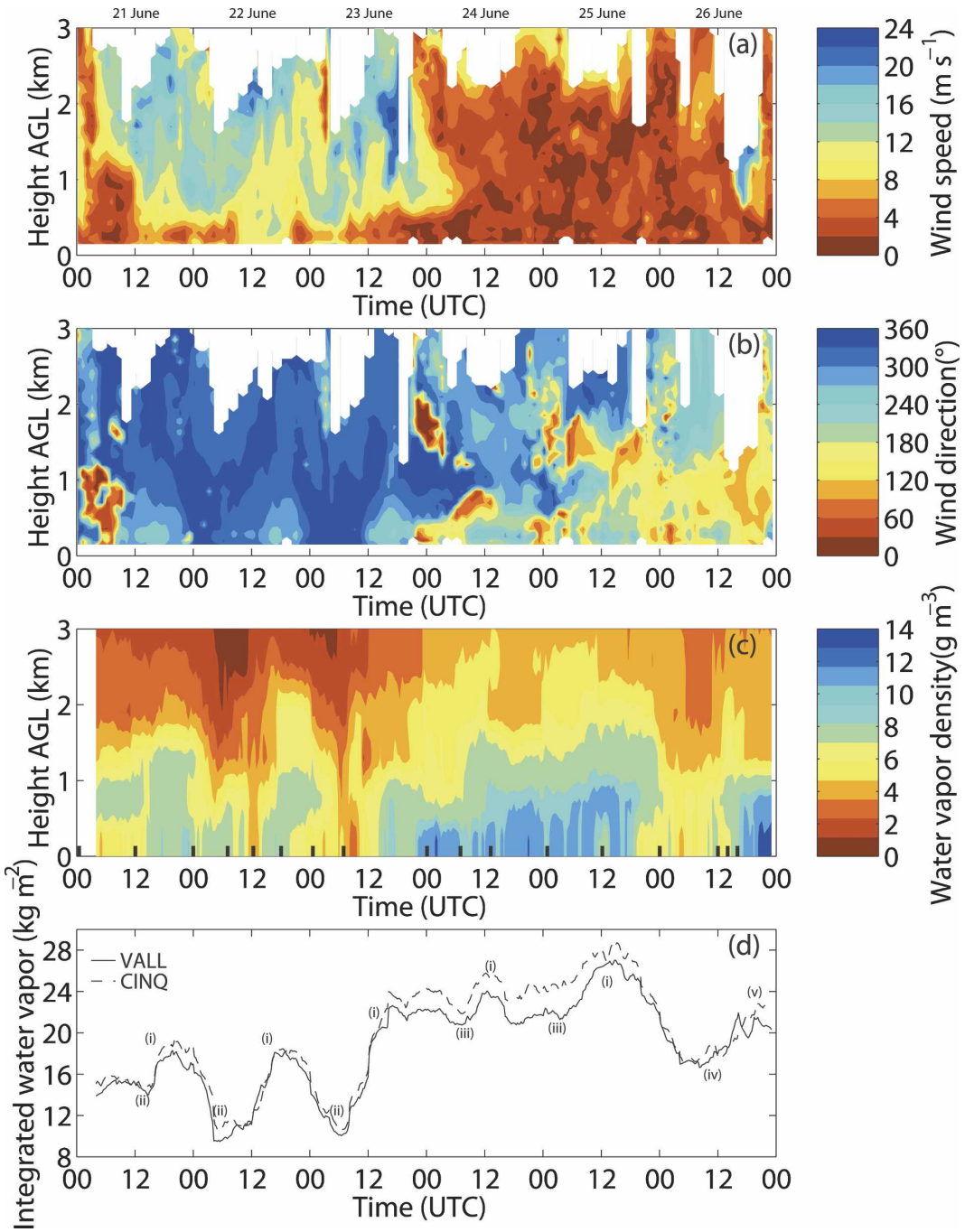

FIG. 5. (a) Time-vs-height plots of wind speed over the center of Marseille (close to the CINQ GPS station; see Fig. 1) as retrieved from the UHF measurements between 21 and 26 Jun. (b) Same as (a), but for the wind direction. (c) Time-vs-height plot of water vapor density retrieved from GPS tomography between 21 and 26 Jun within the Marseille city center at 43.325°N, 5.375°E. The black ticks indicate the times of the assimilated radiosondes. (d) Time series of the IWV from GPS between 21 and 26 Jun at Vallon d'Ol (VALL; northern suburbs of Marseille) and CINQ (Marseille city center). The origin of the IWV variability is indicated as follows: (i) sea breeze advecting inland marine moist air, (ii) mistral advecting continental dry air from the northwest, (iii) land breeze advecting offshore the moist air advected inland by the preceding sea breeze and having experienced cooling and condensation, (iv) easterly synoptic flow, and (v) combination of sea breeze with prevailing continental southeasterly flow.

which tops at more than 3.5 km (not shown), except on 26 June in the presence of an easterly wind regime.

During IOP2a, the dry northwesterly mistral, which blows up to 2–3 km AGL, leads to a much drier free troposphere over Marseille than during IOP2b. The onset of the sea breeze is very late (around 1500 UTC) on 22 June, which limits the daytime accumulation of humidity. The maximum of water vapor is reached at about 1800 UTC, which is consistent with surface-station measurement in the northern suburbs of Marseille (see Bastin et al. 2005). The vertical extension of the "moist" layer (all colors except red) is likely to be induced by the enhanced turbulent mixing, resulting from the detrainment of water vapor from the sea-breeze flow into the free troposphere aloft (Bastin and Drobinski 2006). At night, the dry mistral flow reaches the ground and blows within a 2-km-depth layer, hence exporting most of the water vapor accumulated during daytime. The contrast in total water vapor content and vertical distribution is thus marked between night and day.

During IOP2b, the maximum of water vapor (dark blue color) is reached late in the evening (later than 2200 UTC 23, 24, and 26 June, earlier on 25 June). At night, weak land-breeze circulation blows over Marseille, which partly exports the moist air imported during the day by the sea breeze. The effects of the land breeze are thus not immediate because of its weak intensity. However, the contrast in stratification and total column content of water vapor between day and night is very small. This small contrast during 23 (from midday), 24, and 25 June is due to 1) local radiative cooling and condensation that reduce the amount of water vapor during night (in contrast with the mistral, which advected continental dry air masses on a synoptic scale during IOP2a) and 2) the weakness of the land breeze near the surface (at most 2 m s^{-1}) and of the synoptic flow above (at most 5 m s^{-1}), which are not as efficient as the mistral in exporting the air mass that accumulated moisture during daytime. As a consequence, total column humidity is nearly constant, and in fact it slightly increases between 24 and 25 June. During the night between 25 and 26 June, the dry easterly flow acts as the mistral did during nighttime of IOP2a.

b. Vertically integrated water vapor

Total column humidity, or IWV, is the common atmospheric GPS product that can be retrieved from single stations. It quantifies the amount of water vapor available in the column of atmosphere. This variable is related to the quantity of rain that may eventually fall, though the relationship between IWV and precipitation is not obvious. IWV is generally not easy to interpret alone and requires the combined analysis with surface and upper-air thermodynamic variables. In this case study, IWV time series can be interpreted with the help of a wind profiler (Figs. 5a,b) and vertical moisture distribution from tomography (Fig. 5c). This section thus provides a description and interpretation of IWV using the vertically resolved observations presented in the previous sections.

Figure 5d shows the time series of the IWV from the GPS measurements at CINQ, in the center of Marseille, and VALL, 6 km to the north of the former (Fig. 1c). We first analyze the time series at CINQ. In these time series, the two periods of interest are clearly distinct: 1) the mean IWV over IOP2a is 15.5 kg m^{-2}, whereas it amounts to 21.7 kg m^{-2} during IOP2b; 2) the amplitude of the diurnal variations about the mean IWV are much larger during IOP2a (5, 9, and 12 kg m^{-2} for 21–23 June) than during IOP2b (3.5, 5.5, and 5 kg m^{-2} for 24–26 June). The two special cases of 23 June, marked by the dissipation of the mistral, and 26 June, marked by an easterly wind regime, are discernible.

The lower IWV mean value and the greater amplitude of variations around the mean value during IOP2a are explained by 1) the drier free troposphere over Marseille, 2) the smaller vertical extent of the sea breeze, 3) the later onset of the sea breeze (around 1500 UTC) and peaking of humidity in the boundary layer (around 1800 UTC), which limits the daytime accumulation of humidity, and 4) the transport of humidity offshore during nighttime by the mistral flow, which reaches the ground and blows within a 2-km-depth layer.

During the night from 25 to 26 June, the large decrease of the IWV mean value is mainly due to the large-scale drier continental air blowing from the east. During the daytime of 26 June, this flow veers to the southeast and combines with the sea-breeze flow, hence increasing IWV again by the end of the day. During daytime, the impact of the synoptic-scale flow is very different from IOP2a where the mistral flow blows in nearly the opposite direction to the sea-breeze flow. Also, the maximum IWV is reached late in the evening because this synoptic-scale (southeasterly) flow does not reverse and consequently inhibits the creation of a land breeze (Arritt 1993).

By comparing IWV observed at VALL and CINQ (Fig. 5d), interesting differences are apparent. Actually, CINQ has more IWV throughout the time series but the differences are larger during IOP2b. The differences of IWV are mainly due to the location of the two stations: CINQ station is in the center of the city of Marseille, at an altitude of 131 m above mean sea level (MSL), while VALL is located in the northern suburbs

of Marseille, farther to the coastline, at an altitude of 314 m MSL. The differences of altitude and distance from the coastline create the lower level of IWV at VALL during the whole IOP2. The complex sea-breeze circulation over Marseille induces the stronger differences of IWV during IOP2b. Indeed, during the sea-breeze regime, the SSB has mostly a westerly direction at VALL (see the coastline shape in Fig. 1) while CINQ is in the convergence zone between the two SSBs: the westerly SSB that enters Marseille by its western coast and the southerly SSB that enters Marseille by its southern coast. More moist air consequently reaches CINQ, and IWV values are higher than are observed at VALL. Moreover, the Massif de l'Etoile, culminating at 600 m MSL to the north of Marseille, might induce some flow blocking and thus accumulation of water vapor in the center of the city. This is especially observed during IOP2b, when the diurnal cycle is controlled by the alternation of land and sea breezes.

c. *Horizontal variability*

As discussed above, the temporal evolution of the vertical distribution of water vapor and IWV is strongly linked to horizontal flow in different layers—from the local SSB to the regional DSB and synoptic scale circulation. With the data at hand, the horizontal distribution of water vapor can be analyzed from either horizontal cross sections of water vapor density obtained from the tomographic analyses [as used in Bastin et al. (2005)] or from two-dimensional (2D) maps of IWV. Though the GPS network operated during ESCOMPTE covers a very small area, considerable differences in IWV are observed between stations. We therefore used IWV maps to analyze the evolution of the 2D horizontal distribution of IWV during 22, 25, and 26 June. These maps confirm and complement the analysis from the previous sections.

Figure 6 shows that there is a persistent north–south gradient in IWV, resulting from the local topography (as discussed above). Figures 6a–c show the evolution for 22 June. This is a typical case of sea-breeze development under a moderate mistral. At 0600 UTC, the average IWV is very low (about 10 kg m^{-2}), with a uniform IWV content over the central part of the domain. During this period, the mistral advects dry and cold continental air over the whole domain. At 1200 UTC, the atmospheric boundary layer starts to deepen and moisten, and the mistral flow layer rises because of convective eddies in the convective boundary layer. However, no clear gradient is seen because of the late establishment of the sea breeze over Marseille. The synoptic mistral flow actually inhibits the sea-breeze flow until 1500 UTC. Last, during the afternoon, the sea breeze becomes strong enough to lift the mistral up to 700 or 800 m (Figs. 5a,b). The air then becomes significantly more humid. At 1800 UTC, the IWV content reaches 20 kg m^{-2} over the southern part of the domain and there is a marked north–south, as well as a smaller east–west, gradient. This gradient is a result of the combination of a southerly and westerly inflow, because the SSB blows perpendicular to the local direction of the coastline (see section 3c).

Figures 6d–f provide a similar view for 25 June, which is a typical case of a daily sea-breeze development following a nocturnal land breeze. The average IWV is much higher than in the previous case (about 25 kg m^{-2} at 0600 UTC). At 0600 UTC, there is a strong north–south gradient throughout the domain, which follows the land breeze flow exporting moisture to the sea (mainly to the south). However, as already mentioned, the land breeze is not as efficient as the mistral in drying up the atmosphere (and hence the very large IWV observed at 0600 UTC, about 22–25 kg m^{-2} in the center of the domain). On 25 June, the sea-breeze onset occurs earlier (shortly after sunrise) in the morning than during IOP2a. At 1200 UTC, the SSB blows again from south and west, and IWV is increasing to 30 kg m^{-2} in the central area. At 1800 UTC, the humidity starts to decrease in the western part of the city, in agreement with Fig. 5d wherein the maximum of humidity is observed around 1600 UTC.

Figures 6g–i show a very different IWV pattern and evolution for 26 June. After an overall drop in IWV during the night, the synoptic flow is from east to southeast during most of the day, which combines with the southwesterly sea breeze. At 0600 UTC, the average IWV is about 18 kg m^{-2}, and the gradient is oriented toward the southeast. The average IWV goes on decreasing to 15 kg m^{-2} after 0600 UTC. At 1200 UTC, the gradient is more easterly to the south of the domain, in response to the easterly synoptic flow, and IWV has mostly increased in the eastern part of the domain. Indeed, Lemonsu et al. (2006) show that the air mass that reaches Marseille from the east initially comes from the south over the Mediterranean Sea and it then brings some humidity. Figure 6h shows that IWV has also increased in the western part of the domain, where the westerly SSB enters the city of Marseille. At 1800 UTC, both the easterly–southeasterly gradient and the peak over the city center are reinforced by the persistence of moisture accumulation from both flows.

At this point of the study, model simulation was not mandatory to analyze the GPS data. In this last paragraph, we propose to use the wind fields simulated by Lemonsu et al. (2006) to investigate further the horizontal variability of the vertical profiles of water vapor

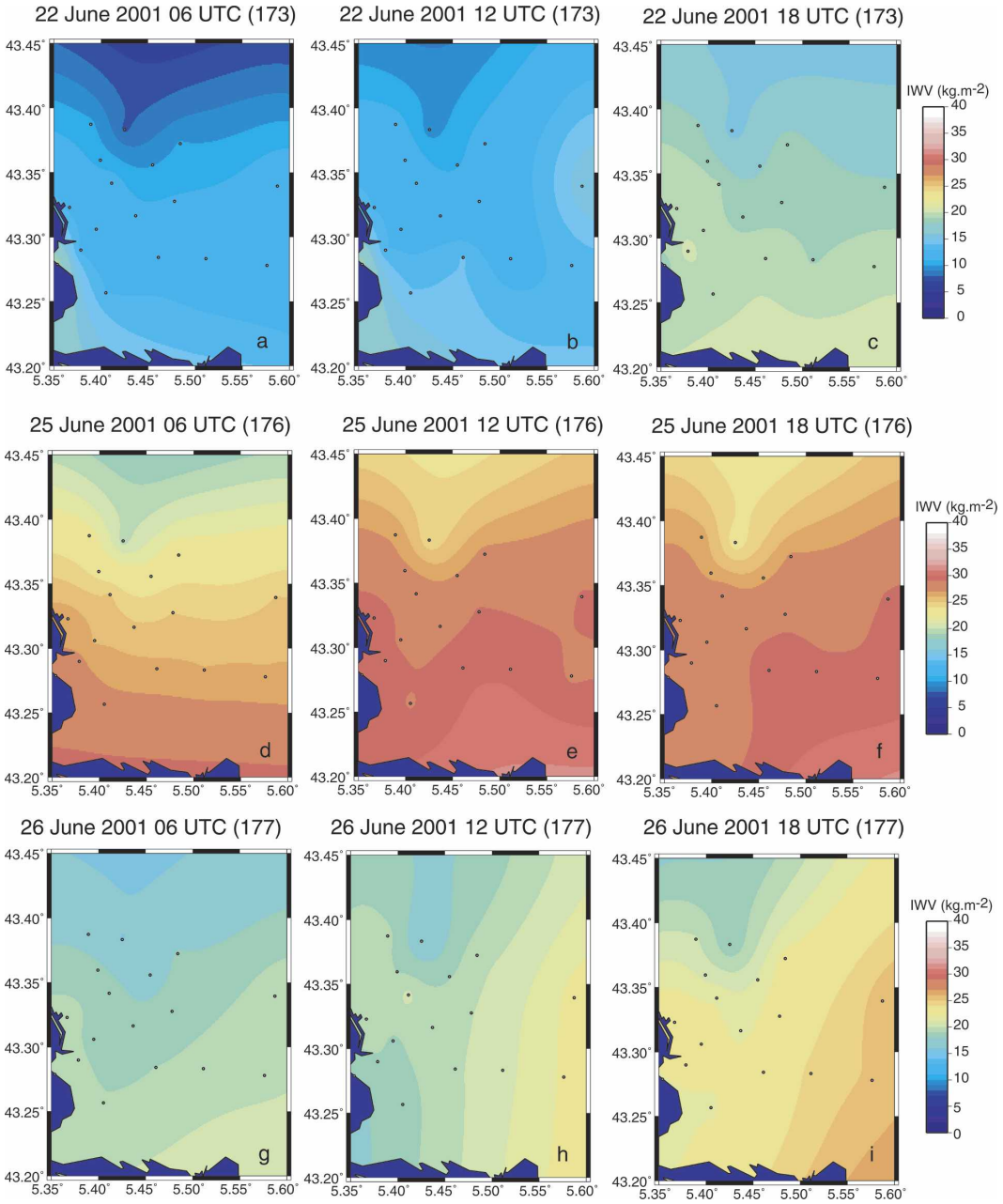

FIG. 6. IWV spatial variations from the ESCOMPTE GPS network at (a) 0600, (b) 1200, and (c) 1800 UTC 22 Jun, (d) 0600, (e) 1200, and (f) 1800 UTC 25 Jun, and (g) 0600, (h) 1200, and (i) 1800 UTC 26 Jun.

density. Figure 7 displays the vertical profiles of water vapor density versus time from GPS tomography at 43.375°N latitude, 5.375°E longitude (Fig. 7a) in the northern suburbs of Marseille, close to VALL station; at 43.275°N latitude, 5.375°E longitude (Fig. 7b), very close to the coastline, in the city core, close to MARS station; and at 43.325°N latitude, 5.425°E longitude (Fig. 7c), in the central eastern part, close to JULY station. In the northern suburbs of Marseille, the westerly shallow sea breeze blows (see Fig. 9 of Lemonsu et al. 2006). It advects a humid and cold air mass from the sea that contributes to the stratification of the lower layer. This stratification is visible on Fig. 7a, with a shallow moist layer in the morning, which is consistent with the shallow boundary layer simulated in Lemonsu et al. (2006). This layer deepens in the afternoon as the deep sea breeze forms and then advects moisture above the shallow sea breeze. As shown by Bastin and Dro-

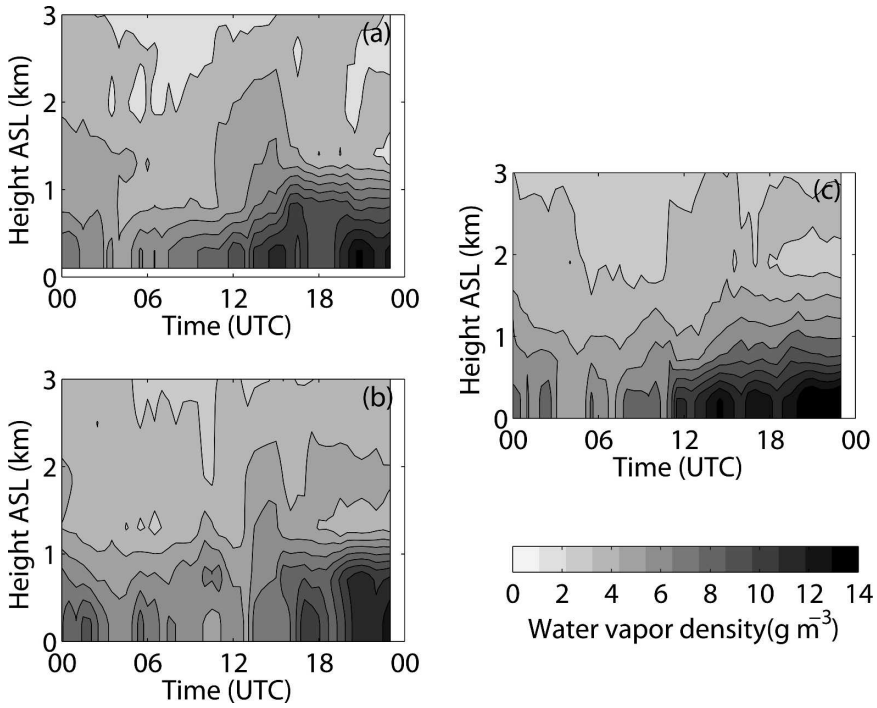

FIG. 7. Time-vs-height plot of water vapor density retrieved from GPS tomography on 26 Jun in the northern suburbs of Marseille at (a) 43.375°N, l 5.375°E, very close to the coastline, (b) 43.275°N, 5.375°E, in the city core, and (c) 43.325°N, 5.425°E, in the central eastern part of the domain.

binski (2005), at VALL, the shallow sea breeze combines with an upslope wind during the day. This combination could contribute to the vertical export of humidity visible in Fig. 7a between 1200 and 1600 UTC. Indeed, while the intensity of the wind along the slope increases, the flow can pump the humid air mass into the free troposphere (e.g., King et al. 1987; Kossmann et al. 1999). Surface station measurements at VALL show that the westerly combination of slope wind and shallow sea breeze suddenly stops at 1600 UTC (the wind direction switches from 270 to 160°), and as a consequence the vertical ventilation stops and the water vapor stays within the boundary layer after 1600 UTC. Close to the MARS station (Fig. 7b), the situation is different. Lemonsu et al. (2006) shows the existence of a wake in this area in the morning, induced by local topography when the south-southeasterly flow enters the south of the city. This region of stagnant air prevents the westerly shallow sea breeze from entering the city at this location, on this day (contrary to 25 June). The air mass at MARS is consequently drier than at VALL in the morning. Also, the lower troposphere is less stratified because of the absence of the shallow sea breeze. In the early afternoon, both the westerly and the southerly shallow sea breezes are stronger and MARS is located near the convergence zone of these two shallow sea breezes. At the convergence front, an updraft is generated, which exports some water vapor in the upper levels (as shown on Fig. 7b) between 1200 and 1500 UTC. Later, the convergence front moves northward, and then the intensity of the updraft decreases at the MARS location. The water vapor progressively accumulates within the boundary layer. In the central part of the domain (Fig. 7c), the humidity can come from both the west and the southeast. The water vapor density starts to increase earlier than in MARS because the humid air mass can reach this station earlier because of the absence of a wake downstream of the low topography. As in VALL, the depth of the moist layer increases during daytime. Contrary to the two other stations, the water vapor is confined within the boundary layer during the whole day because of the absence of a convergence front at this location.

5. Conclusions and perspectives

The first conclusion from this study is that the water vapor variability, even observed in a small domain (20 km × 20 km in our case), has a multiscale nature. Indeed, the water vapor above Marseille has a local origin because it is mainly advected by the shallow sea breeze

that blows near the surface and perpendicular to the coastline shape. However, the large-scale synoptic flow has a strong impact on the content of moisture in the lower troposphere. It can modify the development of the sea-breeze flow (depth, onset time, inland penetration) and its diurnal cycle. It has been shown that the synoptic-scale dry continental mistral wind is very effective at exporting moisture offshore at night that was enhanced by the daily sea-breeze flow. In a similar way, a synoptic-scale flow can also enhance the daily sea breeze and lead to the accumulation of moisture inland. Such a situation was encountered at the end of IOP2 with a southeasterly flow.

The GPS data from ESCOMPTE proved to be valuable for the description of the 4D water vapor variability at small scales. This description was relevant for the analysis of the diurnal cycle of water vapor over the city of Marseille, France. However, GPS data alone are generally not sufficient for a proper comprehension of the atmospheric processes acting in such a case study. The combination of vertical profiles of humidity from GPS tomography and radiosondes with wind profiler data was necessary for understanding the diurnal cycle of water vapor in a typical atmospheric column (in the center of Marseille). The diurnal cycle of IWV from GPS data could then be interpreted properly in the context of the local circulation and the vertical distribution of water vapor density. A comparison between two GPS stations showed that slight differences in the diurnal cycle of IWV can be observed even from nearby stations (6 km apart). This difference could be related to the local topography. It became evident from 2D maps of IWV that a persistent gradient in IWV followed the topography. Gradients in IWV were also related to the direction of the flow in the lower troposphere. The temporal evolution observed in 2D maps also provided important information on the origin of the humid air masses advected from the sea-breeze or synoptic-scale flows.

A second important conclusion is that the different GPS products available from the current experimental data each provided a complementary view of tropospheric water vapor variability. From a methodological point of view it was important to show that much information is contained in the IWV times series and that it can be interpreted in combination with a few other observational data. Also, in this study, GPS tomography has been used for a 3D analysis and not only as a profiler, which is a new step in the use of GPS products.

In this study, the rapid evolution of the vertical distribution of water vapor was provided from GPS tomography with radiosondes, with a 30-min resolution and a 500-m vertical grid size. Only a few other observational techniques can provide such data. One of the main advantages of the GPS technique is its all-weather capability, hence providing a continuous monitoring of the atmosphere. In the case of ESCOMPTE, a well-designed network was deployed. The question to be addressed next is the capability of the GPS tomography technique over larger and sparser networks, such as permanent networks. Another way to exploit water vapor observations from GPS data is to assimilate them in atmospheric models. Significant benefit could be achieved with GPS data if slant delays or SIWV contents would be assimilated, because they provide information on the anisotropy of the water vapor field that is not contained in IWV (Falvey and Beavan 2002; MacDonald et al. 2002).

Acknowledgments. The authors thank A. Walpersdorf and A. Lemonsu for their contribution. The authors are also very grateful to T. Weckwerth and the reviewers for their relevant comments and their help in improving the paper. They are thankful to B. Cros and P. Durand for the coordination of the ESCOMPTE experiment and E. Doerflinger for the coordination of the GPS experiment. They also acknowledge the Institut National des Sciences de l'Univers (INSU) of the Centre National de la Recherche Scientifique (CNRS) through the Programme National de Télédétection Spatiale (PNTS) and the Institut Géographique National (IGN) who supported the GPS field experiment. The ESCOMPTE steering committee and the major French contributors to the ESCOMPTE field campaign [Agence De l'Environnement et de la Maîtrise de l'Énergie (ADEME), Ministère de l'Aménagement du Territoire et de l'Environnement (MATE), INSU, and Météo-France] are also acknowledged. The authors also acknowledge the people from Marseille who kindly agreed to host a GPS receiver in their gardens or on the roofs of their houses.

REFERENCES

Arritt, R. W., 1993: Effects of the large-scale flow on characteristic features of the sea breeze. *J. Appl. Meteor.,* **32,** 116–125.

Banta, R. M., 1995: Sea breezes shallow and deep on the California coast. *Mon. Wea. Rev.,* **123,** 3614–3622.

Bastin, S., and P. Drobinski, 2005: Temperature and wind velocity oscillations along a gentle slope during sea-breeze events. *Bound.-Layer Meteor.,* **114,** 573–594.

——, and ——, 2006: Sea breeze induced mass transport over complex terrain in southeastern France: A case study. *Quart. J. Roy. Meteor. Soc.,* **132,** 405–423.

——, C. Champollion, O. Bock, P. Drobinski, and F. Masson, 2005: On the use of GPS tomography to investigate water vapor variability during a mistral/sea breeze event in south-

eastern France. *Geophys. Res. Lett.,* **32,** L05808, doi:10.1029/2004GL021907.

——, and Coauthors, 2006: On the interaction between sea breeze and summer mistral at the exit of the Rhône valley. *Mon. Wea. Rev.,* **134,** 1647–1668.

Bevis, M., S. Businger, T. Herring, C. Rocken, R. A. Anthes, and R. H. Ware, 1992: GPS meteorology: Remote sensing of the atmospheric water vapor using the global positioning system. *J. Geophys. Res.,* **97,** 15 787–15 801.

Bock, O., and Coauthors, 2004: GPS water vapor tomography project: Description and first results of the ESCOMPTE field experiment. *Phys. Chem. Earth,* **29,** 149–157.

Champollion, C., F. Masson, M. N. Bouin, A. Walpersdorf, E. Doerflinger, O. Bock, and J. Van Baelen, 2005: GPS water vapour tomography: Preliminary results from the ESCOMPTE field experiment. *Atmos. Res.,* **74,** 253–274.

Cros, B., and Coauthors, 2004: The ESCOMPTE program: An overview. *Atmos. Res.,* **69,** 241–279.

Davis, J. L., T. H. Herring, I. I. Shapiro, A. E. E. Rogers, and G. Elgered, 1985: Geodesy by radio interferometry: Effects of atmospheric modeling errors on estimation of baseline length. *Radio Sci.,* **20,** 1593–1607.

Drobinski, P., and Coauthors, 2005: Summer mistral at the exit of the Rhône valley. *Quart. J. Roy. Meteor. Soc.,* **131,** 353–375.

Elgered, G., 1993: Tropospheric radio path delay from ground-based microwave radiometry. *Atmospheric Remote Sensing by Microwave Radiometry,* M. A. Janssen, Ed., John Wiley and Sons, 215–258.

Elòsegui, P., J. L. Davis, L. P. Gradinarsky, G. Elgered, J. M. Johansson, D. A. Tahmoush, and A. Rius, 1999: Sensing atmospheric structure using small-scale space geodetic networks. *Geophys. Res. Lett.,* **26,** 2445–2448.

Emardson, T. R., and H. J. P. Derks, 1999: On the relation between the wet delay and the integrated precipitable water vapour in the European atmosphere. *Meteor. Appl.,* **6,** 1–12.

Falvey, M., and J. Beavan, 2002: The impact of GPS precipitable water assimilation on mesoscale model retrievals of orographic rainfall during SALPEX'96. *Mon. Wea. Rev.,* **130,** 2874–2888.

Flores, A., G. Ruffini, and A. Rius, 2000: 4D tropospheric tomography using GPS wet slant delays. *Ann. Geophys.,* **18,** 223–234.

Foelsche, U., and G. Kirchengast, 2001: Tropospheric water vapor imaging by combination of ground-based and spaceborne GNSS sounding data. *J. Geophys. Res.,* **106,** 27 221–27 231.

Gradinarsky, L., 2002: Sensing atmospheric water vapor using radio waves. Ph.D. thesis, Chalmers University of Technology, Göteborg, Sweden (Tech. Rep. 436).

Guénard, V., P. Drobinski, J.-L. Caccia, B. Campistron, and B. Bénech, 2005: Experimental investigation of the mesoscale dynamics of the mistral. *Bound.-Layer Meteor.,* **115,** 263–288.

Haase, J., M. Ge, H. Vedel, and E. Calais, 2003: Accuracy and variability of GPS tropospheric delay measurements of water vapor in the western Mediterranean. *J. Appl. Meteor.,* **42,** 1547–1568.

Jànsa, A., 1987: Distribution of the mistral: A satellite observation. *Meteor. Atmos. Phys.,* **36,** 201–214.

Jarlemark, P., J. Johansson, B. Stoew, L. Gradinarsky, and G. Elgered, 2001: Spatial error correlations of GPS atmospheres as determined from simulations. *Phys. Chem. Earth,* **26** (A6–8), 451–456.

Jiang, Q., R. B. Smith, and J. D. Doyle, 2003: The nature of the mistral: Observations and modeling of two MAP events. *Quart. J. Roy. Meteor. Soc.,* **129,** 857–876.

Kambezidis, H. D., D. Weidauer, D. Melas, and M. Ulbricht, 1998: Air quality in the Athens basin during sea-breeze and non-sea breeze days using laser-remote-sensing technique. *Atmos. Environ.,* **32,** 2173–2182.

King, J. A., F. H. Shair, and D. D. Reible, 1987: The influence of atmospheric stability on pollutant transport by slope winds. *Atmos. Environ.,* **21,** 53–59.

Koo, Y. S., and D. D. Reible, 1995: Flow and transport modeling in the sea breeze. Part II: Flow model application and pollutant transport. *Bound.-Layer Meteor.,* **75,** 209–234.

Kossmann, M., U. Corsmeier, S. F. J. De Wekker, F. Fiedler, R. Vogtlin, N. Kalthoff, H. Gusten, and B. Neininger, 1999: Observations of handover processes between the atmospheric boundary-layer and the free troposphere over mountainous terrain. *Contrib. Atmos. Phys.,* **72,** 329–350.

Lemonsu, A., S. Bastin, V. Masson, and P. Drobinski, 2006: Vertical structure of the urban boundary layer over Marseille under sea breeze condition. *Bound.-Layer Meteor.,* **118,** 477–501.

Leveque, J.-J., and F. Masson, 1999: From ACH tomographic models to absolute velocity models. *Geophys. J. Int.,* **137,** 621–629.

MacDonald, A. E., Y. Xie, and R. Ware, 2002: Diagnosis of three-dimensional water vapor using a GPS network. *Mon. Wea. Rev.,* **130,** 386–397.

Mayençon, R., 1982: *Météorologie Pratique*. Editions Maritimes et d'Outre-Mer, 336 pp.

Niell, A. E., A. J. Coster, F. S. Solheim, V. B. Mendes, P. C. Toor, R. B. Langley, and C. A. Upham, 2001: Comparison of measurements of atmospheric wet delay by radiosonde, water vapor radiometer, GPS, and VLBI. *J. Atmos. Oceanic Technol.,* **18,** 830–850.

Pettré, P., 1982: On the problem of violent valley winds. *J. Atmos. Sci.,* **39,** 542–554.

Shoji, Y., and Coauthors, 2004: Tsukuba GPS dense net campaign observation: Improvement in GPS analysis of slant path delay by stacking one-way postfit phase residuals. *J. Meteor. Soc. Japan,* **82,** 301–314.

Simpson, J. E., 1994: *Sea Breeze and Local Winds*. Cambridge University Press, 234 pp.

Walpersdorf, A., O. Bock, E. Doerflinger, F. Masson, J. Van-Baelen, A. Somieski, and B. Bürki, 2004: Data analysis of a dense GPS network operated during the ESCOMPTE campaign: First results. *Phys. Chem. Earth,* **29,** 201–211.